# RADIAL DUST DENSITY PROFILES IN SMALL MOLECULAR CLOUDS

JOÃO LIN YUN AND DAN P. CLEMENS
Astronomy Department, Boston University, 725 Commonwealth Avenue, Boston, MA 02215

## ABSTRACT

We have developed a new method for determining the radial volume dust density profiles of dark clouds. We have applied this method to co-added *IRAS* data of 12 small molecular clouds (Bok globules). Raw 60 and 100 μm images were used to generate median filtered backgrounds to be subtracted from the original images. From the resulting differenced images, dust temperature and dust optical depth maps were generated using a single-temperature blackbody model and a dust emissivity proportional to $\lambda^{-1}$. These clouds were resolved at the longest *IRAS* wavelengths and exhibit both regular shapes and structural simplicity. To extract radial dust volume density power laws of the form $n(r) \propto r^{-\gamma}$, a collection of dust optical depth contour levels was fitted with ellipses, and the slope of the run of log (column density) versus log (impact parameter) was determined. Modeling enabled determining a relation between the column density power law and the volume density power law for finite-sized clouds. The volume indices $\gamma$ were found to be in the range 1 to 5/2, in agreement with previous studies of the *gas* density. Our rather soft dust indices do not support the hypothesis of grain settlement into the cores of these clouds. However, given the spread in observed indices, the magnitude of a necessary correction for clouds of finite size, and the uncertainties in using a single-temperature blackbody model for *IRAS* data, determination of the dynamical state of these clouds from *IRAS* data via this method is not currently reliable.

*Subject headings:* infrared: sources — interstellar: grains — nebulae: structure

## 1. INTRODUCTION

Stars in our galaxy generally seem to form as the result of a process of collapse and fragmentation in giant molecular clouds. These clouds, however, are complex, exhibiting clumpiness, turbulence, and multiple episodes of star formation. Thus, they are not the best objects in which to study the early stages of star formation, or in which to probe the physical conditions existing in clouds before star formation takes place. Small molecular clouds (dark clouds) are generally simpler and better suited to this purpose. Bok globules, the smallest dark clouds, are nearby, fairly isolated, and usually display simple or regular shapes. By hypothesizing that these globules were in a state of gravitational collapse, Bok & Reilly (1947) were the first to suggest that these globules might play a role in star formation. Until recently, there has been little evidence for gravitational collapse; indeed the current understanding is that Bok globules exhibit virialized structures (Leung 1985 and references therein). However, from an analysis of short-wavelength *IRAS* co-added survey data we have found a high degree of correlation between Bok globules and young stellar objects (Yun & Clemens 1990).

Because their structures are relatively simple, the small globules are convenient for studying the formation of an individual star, as well as for probing the physical properties present in molecular clouds and cores prior to the onset of star formation. Among these properties, the gas and dust density profiles are important to the basic structure of a molecular cloud. The radial density profile in a cloud determines observational effects such as limb brightening (Lee & Rogers 1987; Leung & O'Brien 1989) or the spectral index of optically thin emission from a centrally heated cloud (Emerson 1988). When the radial dependence of the dust density is expressed in power-law form [e.g., $n(r) \propto r^{-\gamma}$], the power-law exponent $\gamma$ is a useful measure of the degree of dust condensation in these clouds. This characterization allows a direct comparison with similar *gas* density laws (Snell 1981; Fulkerson & Clark 1984; Arquilla & Goldsmith 1985; Frerking, Langer, & Wilson 1987), as well as with determinations of *dust* density laws in Bok globules (Tomita, Saito, & Ohtani 1979; Cernicharo, Bachiller, & Duvert 1985). Also, determination of radial density profiles is of interest as a dynamical probe: the density of an infinite isothermal gas sphere has a radial dependence of $r^{-2}$ if it is in hydrostatic equilibrium (Chandrasekhar 1957), and of $r^{-3/2}$ if it is in free-fall collapse (Shu 1977). Conveniently, a finite, pressure-bounded cloud also retains these density gradients (Arquilla & Goldsmith 1985).

Previous methods of deriving the density structure in dark clouds have adopted simplifying assumptions to obtain the dust density laws $n(r)$. They typically assumed spherical symmetric clouds of infinite extent. However, most real clouds do not exhibit circular column density contours as implied by the spherical symmetry assumption, and finite extents impose a correction to the derived value of the power-law exponent $\gamma$. Here we develop a method that uses ellipses to approximate the cloud column density contours and introduces the necessary correction for the effect of finite cloud radii.

In this paper we describe the study of a set of 12 small molecular clouds selected from the list of clouds cataloged by Clemens & Barvainis (1988, hereafter CB). The global properties of the 248 CB clouds were studied using large-area *IRAS* photometry and $^{12}$CO survey techniques by Clemens, Yun, & Heyer (1991, hereafter CYH). In § 2 we present a description of the *IRAS* data used in this study and the process used to generate dust temperature and dust optical depth images, and discuss the selection of the set of 12 clouds fully probed here. In § 3 the method of analysis is presented. It involves ellipse fitting to contours of dust column density and linear fitting to the radial run of column density to obtain column density power

laws. We then describe our method of deriving volume density indices $\gamma$ from the observed column density power laws. In § 4 we discuss and compare the results found in this work with those of other authors. In § 5 we present a summary of this investigation. The Appendix contains a detailed description of the method of ellipse fitting used in this work.

## 2. DATA

The CB catalog of small molecular clouds contains 248 optically selected small dark clouds (optical size $< 10'$). *IRAS* co-added images of $1° \times 1°$ fields containing these clouds were obtained in each of the four *IRAS* bands for the CYH study. For the present study we used the 60 and 100 $\mu$m images only. Preprocessing of the images consisted of median-filtered background removal. The 100 $\mu$m images (1' pixels) were magnified to match the 60 $\mu$m images (0.5 pixels). Each image was then median-filtered using a large 17.5 kernel and smoothed with a Gaussian of 2.5 width (standard deviation) to build a background image containing the very extended (much larger than each cloud) emission. This background image was then subtracted from the original image. This difference image was then slightly smoothed with a Gaussian of 0.35 width. In this way, a fairly clean and background-subtracted image of the cloud emission was obtained for each of the 248 CB clouds.

### 2.1. Generation of Dust Temperature and Dust Optical Depth Images

The 60 and 100 $\mu$m cleaned images were combined to create images of the dust temperature ($T_{60/100}$) and dust optical depth at 100 $\mu$m ($\tau_{100}$) using a single-temperature blackbody model for these two bands. Emission at 12 and 25 $\mu$m from the clouds was not considered in this study. In fact, as noted in CYH, because of the different dust grain components, the globule *IRAS* average spectrum cannot be represented by any single-temperature blackbody (even modified by normal wavelength-dependent emissivity terms). For a single dust temperature $T$ along each line of sight, the intensity of the optically thin thermal emission from a cloud can be written as

$$I_\nu = B_\nu(T)\tau_\nu , \qquad (1)$$

or by considering the wavelengths of 60 and 100 $\mu$m and taking their ratio,

$$\frac{I_\nu(60)}{I_\nu(100)} = \frac{B_\nu(T, 60)}{B_\nu(T, 100)} \frac{\tau_\nu(60)}{\tau_\nu(100)} . \qquad (2)$$

Equation (2) can be solved for $T$ by adopting a dust emissivity law $\tau_\nu \propto \lambda^{-\beta}$. A $\lambda^{-1}$ dependence is generally assumed for wavelengths in the near- and mid-infrared while a $\lambda^{-2}$ relationship has been shown to hold for wavelengths in the millimeter and submillimeter region (e.g., Draine & Lee 1984; Chini, Krugel, & Kreysa 1986). We have tested the effect of different dust emissivity laws ($\beta = 1, 2$) and found no significant differences in the dust density power-law exponents $\gamma$ (see also CYH). A different dust emissivity law produces different temperatures at each point of the cloud, but the inferred radial density gradient is nearly unchanged. Hence, in this study we have assumed $\beta = 1$.

Once equation (2) has been solved for $T$, equation (1) can be used to obtain the optical depth $\tau$. Note that we have assumed that the same population of grains contributes to the 60 $\mu$m and the 100 $\mu$m emission (a rather poor assumption; cf. Heyer et al. 1989). However, because of the way *IRAS* fluxes were

reconstructed and the width of the *IRAS* filters, equation (2) must be replaced by

$$\frac{I_{\nu_1}}{I_{\nu_2}} = \frac{K_{\nu_1} \lambda_{\nu_1}^{-\beta} B_{\nu_1}(T)}{K_{\nu_2} \lambda_{\nu_2}^{-\beta} B_{\nu_2}(T)} , \qquad (3)$$

where $K_\nu$ is the color correction factor (*IRAS* Explanatory Supplement 1988), given by

$$K_{\nu_0}(T) = K_{\lambda_0}(T)$$
$$= \lambda_0^{4+\beta} \left[ \int \frac{R_\lambda}{\lambda^{5+\beta}} \frac{\exp(1.44 \times 10^4/\lambda_0 T) - 1}{\exp(1.44 \times 10^4/\lambda T) - 1} \, d\lambda \middle/ \int \frac{R_\lambda}{\lambda} \, d\lambda \right] , \qquad (4)$$

where $R_\lambda$ is the filter-detector response and $\lambda$ is in microns.

Since equation (3) cannot be solved explicitly for $T$, this equation was instead used to compute a lookup table, which for each value of log $(I_{60}/I_{100})$ gives a value for $T_{60/100}$ (CYH). This lookup table was used in conjunction with the fluxes found at each pixel in the 60 and 100 $\mu$m images to generate the dust-temperature images. Within the set of clouds studied, the temperatures observed were in the range 20–42 K. Similarly, the 100 $\mu$m emission images and the temperature images were used to generate the dust optical depth images ($\tau_{dust}$), using equation (1).

### 2.2. Selection of Clouds for Radial Density Analysis

Dust temperature and dust optical images were generated for each of the 248 CB clouds as described above. By examining the dust optical depth images, it became clear that a large number of the CB clouds were unsuitable for a study of radial density laws. The large size of the *IRAS* detectors meant that clouds of small size ($< 4'$ in the infrared maps) were unresolved. A second reason for rejecting clouds was the obvious presence of strong local heating. Such embedded objects could produce strong deviations from the single-temperature blackbody assumption. However, a few clouds, with evidence for very moderate levels of local heating, have been included. These were relatively large clouds, and the analysis was restricted to portions of the cloud well away from the area of local heating. A third major reason for exclusion of clouds was the irregularity of the infrared optical depth contour levels. In summary, clouds whose dust optical depth images were large ($> 4'$), fairly regular (to enable elliptical contour fitting), and showing little evidence of embedded point sources were selected. In Table 1

TABLE 1
OBSERVED AND INFERRED EXPONENTS OF THE RADIAL DENSITY LAW
$n(r) \propto r^{-\gamma}$ FOR SELECTED CLOUDS

| Cloud (CB) | Right Ascension (1950.0) | Declination (1950.0) | $R_{adopted}$ | $\gamma_0 \equiv 1 + |s|$ [a] | $\gamma$ |
|---|---|---|---|---|---|
| 003 | $0^h 26^m 00^s$ | $56°25'33''$ | 9' | 2.9 (0.1) | 2.7 |
| 028 | 5 03 51 | $-04\ 00\ 00$ | 8 | 1.7 (0.1) | 1.3 |
| 029 | 5 19 42 | $-03\ 44\ 24$ | 8 | 1.8 (0.1) | 1.3 |
| 030 | 5 27 04 | 05 42 45 | 13 | 2.3 (0.1) | 2.1 |
| 056 | 7 12 32 | $-25\ 03\ 38$ | 5 | 1.6 (0.1) | 1.0 |
| 063 | 15 48 11 | $-03\ 57\ 14$ | 9 | 2.0 (0.1) | 1.8 |
| 069 | 16 59 26 | $-33\ 12\ 45$ | 8 | 1.9 (0.1) | 1.3 |
| 088 | 17 25 35 | $-25\ 13\ 52$ | 8 | 1.8 (0.1) | 1.3 |
| 203 | 19 41 43 | 18 57 45 | 7 | 2.1 (0.2) | 1.5 |
| 206 | 19 44 11 | 18 55 07 | 9 | 1.6 (0.1) | 1.2 |
| 217 | 20 05 54 | 36 57 07 | 6 | 1.7 (0.1) | 1.1 |
| 218 | 20 10 42 | $-01\ 30\ 00$ | 10 | 2.5 (0.1) | 2.3 |

[a] $s = d \log N/d \log p$.
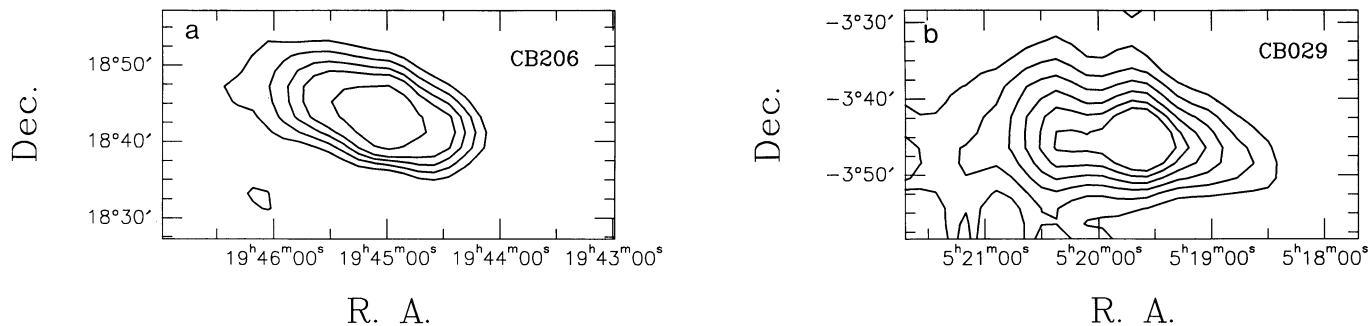
Fig. 1.—Contour plots of dust optical depth ($\tau_{\text{dust}}$) for two clouds selected for this study. (*a*) CB 206; contours are at 2.1, 2.4, 2.7, 3.0, and 3.6 (in units of $10^{-5}$). (*b*) CB 29; contours begin at $1.2 \times 10^{-5}$ and are stepped by $0.3 \times 10^{-5}$.

the 12 clouds selected are listed by CB number and coordinates. Figure 1 shows examples of the dust optical depth contour plots for two clouds selected for this study (CB 206, CB 29).

### 3. ANALYSIS

The dust optical depth $\tau_{\text{dust}}$ is proportional to the dust column density $N_{\text{dust}}$. As a result, for the purpose of this study, the optical depth maps can be considered column density maps. Hence, the quantity which is directly accessible is the dust column density $N$, along a certain line of sight whose "impact parameter" (or projected radius, i.e., the minimum distance to the line of sight from the cloud center) is $p$. The process of determining volume density power laws can then be divided into three steps: (1) determination of the impact parameters $p_i$ for a set of values of the column density $N_i$, yielding a set of data pairs ($p_i$, $N_i$); (2) determination of the least-squares linear slope in the (log $p$, log $N$) plot, yielding a *column* density power law; (3) determination of a correction to convert the exponent found for the *column* density power law into the exponent of the *volume* density power law.

### 3.1. *Ellipse Fitting*

In previous studies, the association of impact parameters with column densities was made using the assumption of global spherical symmetry (circular column density contours, e.g., Frerking et al. 1987). Examination of the plots of column density $N$, in Figures 1*a* and 1*b* is sufficient to conclude that the shapes of the contours are not circular. Furthermore, CB found a mean ellipticity (ratio of the lengths of the major and minor axes) of 2 for the optically opaque cores of these clouds. Thus, the large majority of small clouds are not spherical.

We have developed a method of fitting ellipses to contours of constant column density. These elliptical fits better represent the column density distributions for the clouds. The fitting procedure returns the values of the lengths of the semimajor and semiminor axes of the best-fit ellipse, the coordinates of the center of the ellipse, and the position angle of the ellipse. The ellipse-fitting procedure is fully described in the Appendix. It consisted of determining the ellipse which best fits a curve of constant intensity (contour level) defined in a two-dimensional distribution of pixel values.

For each of the selected clouds, we have examined the cloud contour plots and chosen a range of column densities corresponding to radii as large as possible but still composed of contour levels which appeared regular enough to be well represented by ellipses. The column density step between two consecutive levels was selected to be small (in order to yield many

samples of the radial column density variations) but large enough so as not to oversample the angular resolution or noise levels of the *IRAS* co-added maps. Our ellipse-fitting procedure was then used to fit ellipses to the set of contour levels contained in that range.

The goodness of each fit was checked by plotting the contour level and the fitted ellipse. Figure 2 shows an example of how the contours of CB 206 have been approximated by elliptical contours. In this figure, as a result of approximating each contour level by a fitted ellipse, some of the ellipses cross one another. This has no physical meaning and does not affect the determination of the radial density gradients because this determination does not use all the information contained in the fitted ellipse but only the values of the lengths of its axes. In general for the clouds, except for a few of the most irregular contours, the fit achieved was usually judged to be good to excellent.

### 3.2. *Column Density Power Laws*

The procedure of fitting ellipses to contour levels yielded a set of values $\{x_0, y_0, a, b, \theta\}$ for each contour of constant column dust density $N$. The impact parameter $p$ was then approximated by the geometric mean, $(ab)^{1/2}$, of the lengths of the semimajor and semiminor axes. Although this approach removes some information about the ellipticity of the cloud, it is superior to assuming circular symmetry. The circular symmetric approach typically uses azimuthally averaged column densities to represent the column density at each radius. Here we obtain a more accurate description of the column density through the elliptical fitting. An analysis of the radial dependence along the two independent directions of the major and minor axes would require a model of the volume density law
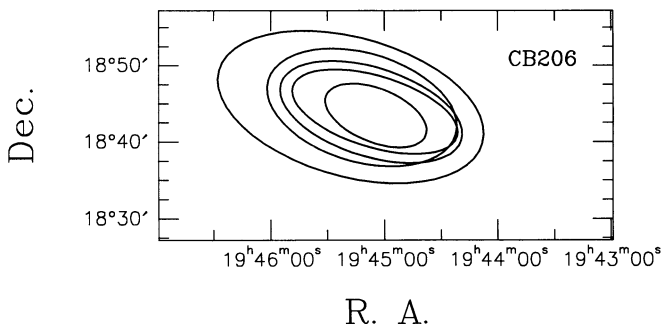


Fig. 2.—Example of the result of the ellipse-fitting procedure for CB 206. The curves shown are the best-fit ellipses to the contours of Fig. 1*a*.

for each cloud which is more complex than a simple power law with radius. By adopting $p = (ab)^{1/2}$ for each contour level of column density value $N$, we are including all the positions belonging to that contour level and associating with these positions an impact parameter that is a representative average of their impact parameters.

Hence, the ellipse-fitting procedure is used to produce a run of data pairs, $\{(p, N)_i\}$, for each cloud. Figure 3 shows the plot of (log $p$, log $N$), as well as the linear least-squares fits to the points in this plane, for each of the clouds. In this figure, $s$ is the slope of each line, i.e.,

$$s = \frac{d \log N}{d \log p}.$$ (5)

Hence, we have $N(p) \propto p^{-\alpha}$ with $\alpha = |s|$.

### 3.3. Relation between $N(p) \propto p^{-\alpha}$ and $n(r) \propto r^{-\gamma}$

In previous works it was generally assumed that the exponent $\gamma$ of the volume density law $n(r) \propto r^{-\gamma}$ could be obtained

by adding unity to the absolute value of the column density slope $\alpha$, i.e., that $\gamma = 1 + \alpha$ (Tomita et al. 1979). For the purposes of comparison, let us define this value of $\gamma$ as $\gamma_0 \equiv 1 + \alpha$. In the fifth column of Table 1 we list the values of $\gamma_0$, derived from the ellipse fitting for each cloud. The uncertainties listed correspond to the uncertainties of the fitted slopes of the (log $p$, log $N$) lines. We note, however, that the total uncertainty (due to image noise, contour plotting, and ellipse fitting) is likely to be higher.

The assumption that the true $\gamma$ coincides with $\gamma_0$ is valid only for a cloud with infinite radius, as will be shown below. In Figure 3 some of the clouds exhibit the presence of a curvature of the data points with increasing $p$ away from the line, which seems to indicate a steeper power law at larger impact parameters. This is most likely due to the proximity of the edges of the clouds. If a simple volume density power law, $n(r) \propto r^{-\gamma}$, is appropriate for these clouds, the proximity of the edge of a cloud will produce the downward curvature of the *column* density $N(p)$ for large impact parameters $p$ (see below). Hence,
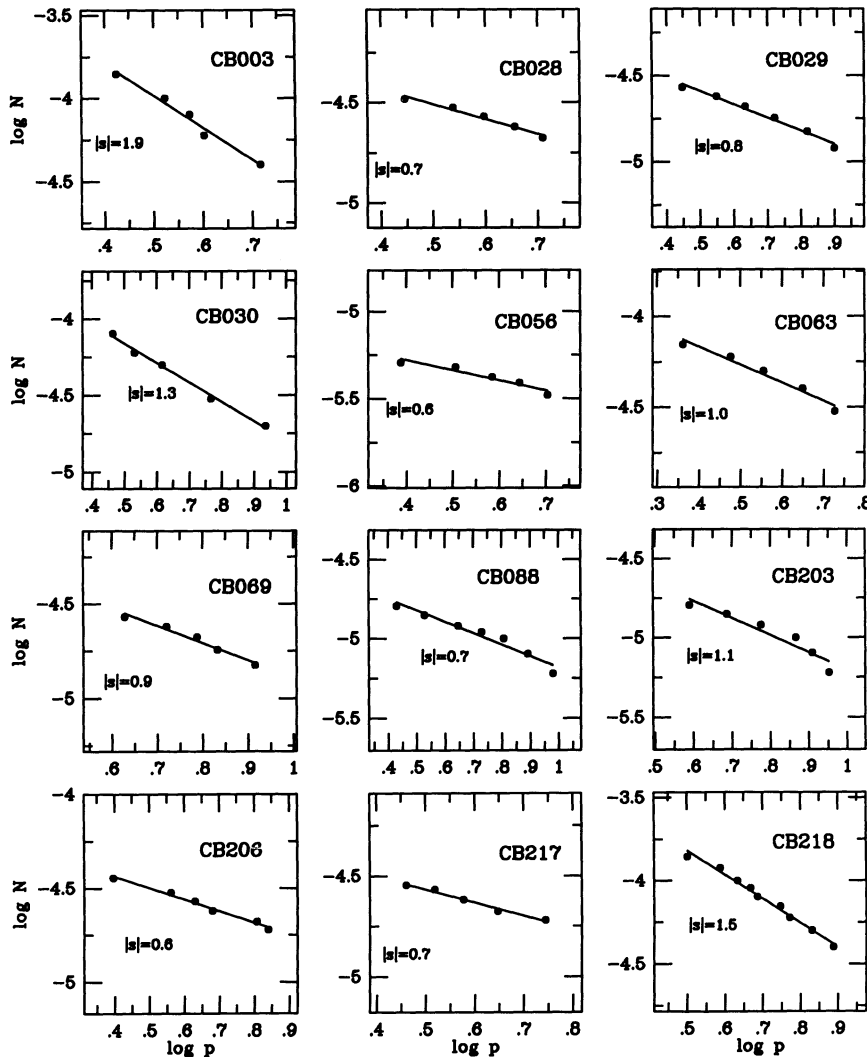


FIG. 3.—Plots of log $N$ vs. log $p$ for the 12 selected clouds. The straight lines are least-squares fits to the points shown. The slopes of the lines are indicated as $|s|$-values. Note the presence of curvature of the data points away from some of the lines for larger radii. This is an indication of the proximity of the cloud edges (see text).

TABLE 2

COLUMN DENSITY EQUATIONS FOR VOLUME DENSITY POWER LAWS WITH INTEGER INDICES

| Volume Density Power-Law Index $\gamma$ $[n(r) \propto r^{-\gamma}]$ | Column Density Dependence | Column Density Dependence on $p$ when $R \to \infty$ |
|---|---|---|
| 0 | $N(p) \propto R(1 - p^2/R^2)^{1/2}$ | [a] |
| 1 | $N(p) \propto \ln \dfrac{R + (R^2 - p^2)^{1/2}}{p}$ | [a] |
| 2 | $N(p) \propto \dfrac{1}{p} \arctan \dfrac{(R^2 - p^2)^{1/2}}{p}$ | $N(p) \propto p^{-1}$ |
| 3 | $N(p) \propto \dfrac{(R^2 - p^2)^{1/2}}{Rp^2}$ | $N(p) \propto p^{-2}$ |
| 4 | $N(p) \propto \dfrac{(R^2 - p^2)^{1/2}}{2R^2p^2} + \dfrac{1}{2p^3} \arctan \dfrac{(R^2 - p^2)^{1/2}}{p}$ | $N(p) \propto p^{-3}$ |

[a] $N(p)$ diverges.

the simple assumption that $\gamma$ equals $1 + \alpha$ will fail as a way of obtaining the true volume density exponent $\gamma$.

### 3.4. *Effects of Finite Cloud Radius*

In order to relate the observed index $\gamma_0$ to the desired index $\gamma$, and given that we approximated the impact parameter $p$ by the geometric mean, $(ab)^{1/2}$, we next modeled the expected runs of ($\log p$, $\log N$) for the case of a spherically symmetric cloud, with $n(r) \propto r^{-\gamma}$. For any line of sight through a cloud of finite radius $R$,

$$N(p) \propto \int_0^{X_R} (x^2 + p^2)^{-\gamma/2} \, dx , \qquad (6)$$

where $X_R = (R^2 - p^2)^{1/2}$. A numerical calculation of $N(p)$ was performed for a fixed value of $p$. A set of such calculations yielded a plot of the run of $N$ with $p$ for each value of $R$ and $\gamma$ chosen. Numerical integrations were needed for the case of noninteger $\gamma$. For integer $\gamma$, Table 2 indicates how $n(r)$ and $N(p)$ are related. A volume density power law $n(r) \propto r^{-\gamma}$ will only yield a column density power law whose exponents differ by unity for all $\gamma > 1$ and where $R \to \infty$.

Figure 4 shows the predicted data points ($\log \xi$, $\log N$) corresponding to $\gamma = 2$, i.e., a power law $n(r) \propto r^{-2}$, where $\xi = p/R$. A best-fit line of slope $|s| = 1.6$ is also shown. The presence of a downward curvature to the data points, relative to the line as $\xi$ approaches unity is clear. Therefore, under the assumption that simple volume density power laws are appropriate for these clouds, the presence of curvature in the plots of Figure 3 is a direct consequence of the finite radii of the clouds.

Figure 4 shows that $1 + |\text{slope}| = \gamma_0 \neq \gamma$. For the specific set of values of $\xi$ used in this figure, the slope of the line is $-1.6$ and, therefore, $1 + |\text{slope}| \neq 2$. In other words, a cloud with a radial volume density law proportional to $r^{-2}$ ($\gamma = 2$) will produce an empirical ($\log \xi$, $\log N$) plot with a least-squares line having a slope of $-1.6$, giving a value of $\gamma_0 = 2.6$. However, this difference between $\gamma$ and $\gamma_0$ ($\Delta \gamma \equiv \gamma - \gamma_0$) may provide a way of inferring the true value of $\gamma$ from the observed value of $\gamma_0$. For the conditions of Figure 4, a set of empirical data points yielding a slope of $-1.6$, and hence a value of $\gamma_0 = 2.6$, would indicate a true volume density power law with $\gamma = 2$, i.e., $\Delta \gamma = -0.6$.

We have generated a set of model plots, similar to Figure 4, but for a range of values of $\gamma$ and for different distributions of values of $\xi$. In each case, we obtained a correspondence between the value of $\gamma_0$, inferred from the least-squares fit to the modeled points, and the input value of $\gamma$ that produced those points. The information contained in this large number of model plots was analyzed in two ways.

First, by considering the subset of model plots obtained with fixed values of $\gamma$, but different values of $\xi$, we have verified that $\gamma_0$ approaches $\gamma$ as $R$ increases relative to the volume of the cloud probed for the column density variation. In Figure 5 we show this result for a fixed value of $\gamma$ ($\gamma = 2$) and a specific set of values of $\xi$. We define $\xi_{max} = p_{max}/R$, where $p_{max}$ is the largest value of the impact parameter sampled. Hence, as $\xi_{max}$ decreases, a smaller *fraction* of the cloud volume is probed with ($\log p$, $\log N$) points. We find that $\gamma_0$ is close to $\gamma$ for small values of $\xi_{max}$, that is, as long as the last sample point is well within the edge of the cloud ($p_{max} \ll R$).

Second, by taking one specific set of values of $\xi$ and varying the input values of $\gamma$, we obtained a set of points ($\gamma$, $\gamma_0$), which are plotted in Figure 6. Each of the data points in this figure was obtained for a specific run of values of $\xi$ labeled by a
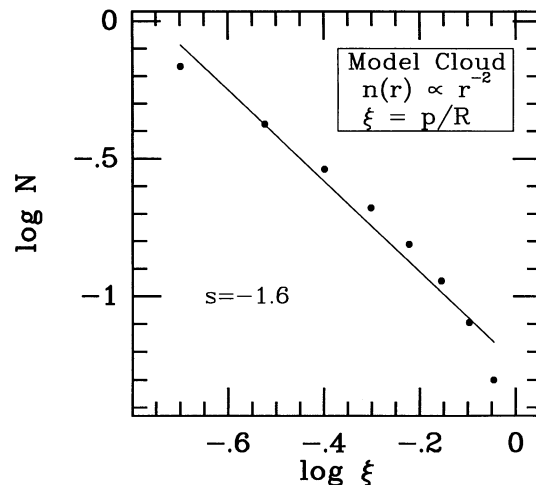


FIG. 4.—Theoretical ($\log \xi$, $\log N$) plot computed for a cloud of radius $R$ in which the power-law relation, $n(r) \propto r^{-2}$, holds. The radial coordinate is $\xi_i = p_i/R$. The least-squares fit line of slope $|s| = 1.6$ is shown. Note the downward curvature of the data points relative to the line as $\xi \to 1$.
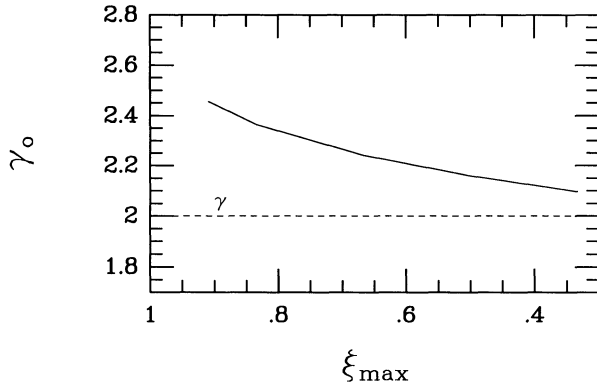
FIG. 5.—Plot of $\gamma_0 \equiv 1 + |s|$ against $\xi_{max}$, for a given set of impact parameters, where $s$ is the slope of the least-squares fit line in the (log $\xi$, log $N$) plot, $\xi_{max} = p_{max}/R$, and $R$ is the radius of the cloud. Note that $\gamma_0 \rightarrow \gamma$ when $R \rightarrow \infty$, as expected.

parameter $\lambda$. This parameter defines a specific set of model column density and impact parameter data points for fitting, indexed as a set of values of $\xi$ as

$$\xi_i = \{i/\lambda : i = 1, 2, \ldots, 10\} . \tag{7}$$

Note that larger values of $\lambda$ correspond to smaller values of $\xi_{max}$, and will therefore produce a smaller cloud edge proximity correction, $\Delta\gamma$. In addition, (1) for the same set of values of $\xi$, $\gamma_0$ is closer to $\gamma$ for large values of $\gamma_0$, hence the $\Delta\gamma$ correction due to finite radius is less important for larger values of $\gamma_0$; and (2) $\gamma_0$ is always an upper limit to the true $\gamma$ ($\Delta\gamma < 0$, always).

The information contained in Figure 6 is presented in Figure 7 as a plot of $\Delta\gamma$ versus $\gamma_0$. This figure can be used to correct the exponents $\gamma_0 = 1 + |s|$ for the effect of finite cloud radius. As an example of this correction process, consider a cloud whose radius is 0.3 pc. For 10 evenly spaced points, the last at an impact parameter of 0.15 pc ($p_{max} = 0.15$ pc), the value of $\lambda$ is 20. Assume also that column density probes of the cloud return the value $|s| = 1.0$. Then, $\gamma_0 = 2.0$, and Figure 7 gives $\Delta\gamma = -0.2$. Hence, $\gamma = 1.8$.
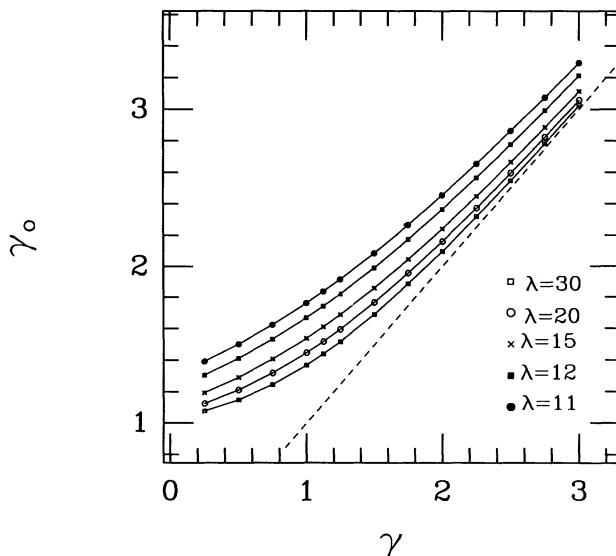


FIG. 6.—Plot of $\gamma_0$ vs. $\gamma$, for different sets of values of $\xi$ specified by the parameter $\lambda$ by $\{\xi_i\} = \{i/\lambda, i = 1, \ldots, 10\}$.

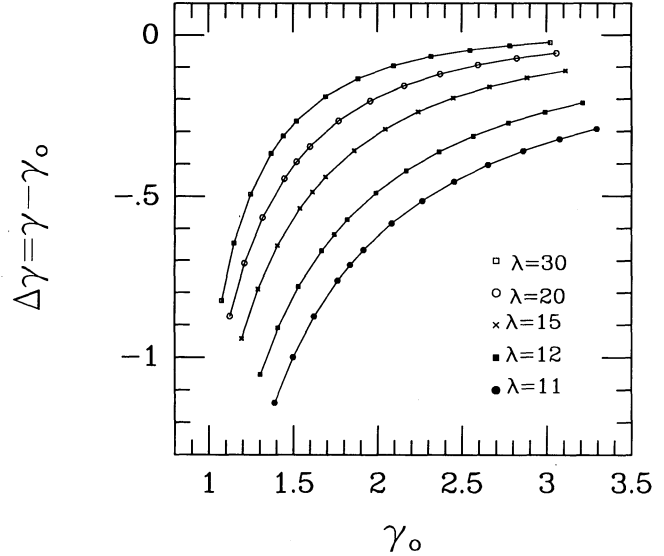

FIG. 7.—Plot of $\Delta\gamma = \gamma - \gamma_0$ vs. $\gamma_0$, for different sets of values of $\xi$ specified by the parameter $\lambda$ by $\{\xi_i\} = \{i/\lambda, i = 1, \ldots, 10\}$. This figure (adapted for the specific run of values of $\xi$ contained in the data) can be used to correct for the effect of finite cloud radius.

Using Figure 7 (adapted for the specific runs of values of $\xi$ contained in our observed cloud data), we determined the true volume density power law for each of the selected clouds, corrected for the effect $\Delta\gamma$ of finite cloud radii. The cloud radii were estimated by viewing the maps of optical depth and typically adopting the geometric mean of the longest and the shortest axes. The adopted values of the cloud radii (in arcminutes) are presented in Table 1. The final, $\Delta\gamma$-corrected values of the true dust density power-law index $\gamma$ are presented in the last column of Table 1.

## 4. DISCUSSION

A histogram of the empirical values of $\gamma_0$ and the model matched values $\gamma$ found in this study are presented in Figure 8. The correction for finite cloud radius shifts all clouds to lower values of $\gamma$, indicating a less steep power law than would be inferred without the correction. We find corrected exponents in the range $-1$ to $-5/2$, with 75% of the clouds between $-1$ and $-2$. A simple mean yields $\gamma = 1.6 \pm 0.2(1 \sigma)$.

Adopting a single dust temperature along each line of sight is a poor assumption because there are likely temperature gradients along the line of sight. From equation (1) we see that the *IRAS* emission has a stronger contribution from the warmer dust. However, over the projected extents of the clouds studied, the observed temperature ($T_{60/100}$) variation was small ($\Delta T/T < 0.2$) with the temperature increasing outward (clouds heated by the interstellar radiation field, and without strong internal heat sources). This implies that the absolute values of the density exponents derived are upper limits to the true density exponents. In other words, if the actual temperature increases outward, the single-temperature model will yield artificially steeper density laws. Using the expression derived by Langer et al. (1989), we estimate that the correction in the exponent due to small temperature gradients ($\Delta T/T < 0.2$) is less than 0.3, for temperatures of the order of 20 K.

In order to investigate our sensitivity to steep power laws in the *IRAS* maps, we have determined the radial variation of the emission intensity of an average representative point source at
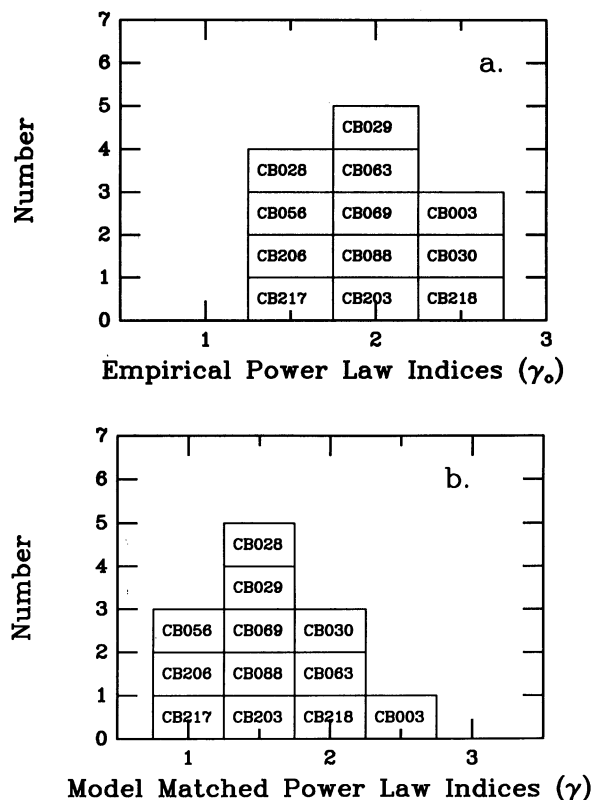
FIG. 8.—Histograms of (a) the raw power index $\gamma_0$ (uncorrected for the effect of finite cloud radius) and (b) the corrected power index $\gamma$, found for the clouds. The correction for finite cloud radius shifts most clouds to lower values of $\gamma$. In both cases, the values found are restricted to a relatively narrow range of values, between 1 and 5/2.

60 $\mu$m. The intensity decreased approximately as $p^{-2}$ ($\gamma_0 \approx 3$). Thus, if the volume density power laws of the clouds were steeper than $r^{-3}$, the histograms of Figure 8 would show a concentration of clouds at the right end of the diagrams, piling up near $\gamma = 3$ (our steepness limit). Since this is not the case, we conclude that power indices steeper than about $-3$ are rare or absent.

These results are in fair agreement with most studies of gas density laws. These studies have consisted of using molecular transitions (CO; Arquilla & Goldsmith 1985; CO and $H_2CO$, Snell 1981) to measure gas column densities in several dark cloud envelopes. These different studies have found most gas density structures to be consistent with $\gamma \approx 2$.

Tomita et al. (1979) applied a star-count technique to POSS images of 12 dark clouds to measure the visual extinction of background starlight. They found steep power-law exponents, in the range of $-3$ to $-5$, indicating strong central condensations. However, Cernicharo et al. (1985), probed the density structure of dark clouds in the Taurus-Auriga-Perseus complex using the same star-count technique. Cernicharo et al. (1985) found $\gamma = 1.3 \pm 0.2(3\,\sigma)$ as the best fit to their data. They estimate that their results are valid for the envelopes of clouds with radii between 0.1 and 1 pc.

The clouds in this study exhibit smaller (softer) values of $\gamma$ than were found by Tomita et al. (1979), but ones which are in good agreement with those of Cernicharo et al. (1985). Hence, we conclude that the notion that dust density laws are strongly steeper than gas density laws is incorrect. Furthermore,

because no strong difference was found between gas and dust radial density laws, it is likely that radiation pressure does not play an important role in determining the equilibrium configuration of the dust (William & Bhatt 1982) in the globules studied here. This result may not be valid for globules with a strong internal heat source which were excluded from this study.

Low values of $\gamma$ can help explain the absence of strong thermal coupling between the gas and the dust in these globules, as discussed by Leung (1985) and found by CYH. A small value of $\gamma$ keeps the local density at most cloud radii close to the mean density ($\approx 10^4$ cm$^{-3}$), which is below the value of $\approx 10^6$ cm$^{-3}$ required for thermal coupling.

Theoretical studies of density profiles in isothermal clouds predict an exponent of $-2$ for equilibrium conditions (cf. Chandrasekhar 1957; Larson 1969; Penston 1969). Interestingly, the self-similar model of cloud collapse developed by Shu (1977) applies well to the physical conditions in Bok globules (low internal temperatures, small masses, subsonic flows, and pressure-bounded objects). This model predicts an $r^{-2}$ law for the density distribution in the nearly static outer envelope, and an $r^{-3/2}$ law for the freely falling inner envelope. Our results are in accord with these predictions. However, given the uncertainties involved in the determination of the density-law exponents, we believe that is not yet possible to describe the dynamical state of these clouds reliably using IRAS data alone. In addition, comparisons with theoretical models should be regarded with caution because these do not include the effects of rotation, magnetic fields, or clumpiness, all of which probably affect the dynamics of real clouds.

Interestingly, the values found for $\gamma$ in most studies of gas and dust using a variety of methods are similar and are restricted to a relatively narrow range. This similarity may provide the basic support for the existence of a linear relation between visual extinction and gas column density in these clouds. Furthermore, the narrow range of density laws found seems to indicate that small dark clouds with extreme density structures are rare.

The method developed in this study to obtain radial volume density power laws is an important improvement over previous attempts. However, the increased complexity of this method, namely, the ellipse-fitting procedure together with the correction for finite cloud radius, are only fully justified when used with higher quality data (better angular resolution and higher signal-to-noise ratio than are used in this study) and larger cloud sizes. Such improvements would help in satisfying the conflicting requirements of using points at large distance from the cloud edge but at impact parameters large enough to be meaningful, given the large IRAS beam size. This technique, coupled with highly resolved far-infrared cloud images generated, for example, by ISO or SIRTF, will decisively address the internal dynamics of dust in these clouds.

## 5. SUMMARY AND CONCLUSIONS

We have developed an improved method of determining the radial volume dust density distribution of small clouds. We have applied this method to 12 small molecular clouds observed by IRAS. IRAS co-added survey images containing these clouds have been analyzed to generate dust temperature and dust optical depth contour plots. Our method included fitting ellipses to contour levels of constant column density to determine the run of column density with impact parameter. Under the assumption of a simple volume density power law

with radius, $n(r) \propto r^{-\gamma}$, we have investigated the relation between the exponent $\gamma$ and the slope $s$ of the least-squares fit to the (log $p$, log $N$) data. We found that corrections for the effect of a finite cloud radius ($\Delta\gamma = \gamma - \gamma_0$; $\gamma_0 = 1 + |s|$) may be large. In addition, we have found the following:

1. The clouds selected for this study have true volume density power indices in the range $-1$ to $-5/2$ (75% between $-1$ and $-2$), similar to values found in studies of the *gas* density laws.

2. The dust density laws found here are flatter than those determined from star counts by Tomita et al. (1979), but in fair agreement with the star-count results of Cernicharo et al. (1985).

3. There is no evidence (of the form of power-law indices near or steeper than 3) for grain settlement into the cores of these clouds.

4. The detailed dynamical state of any particular cloud is difficult to ascertain from *IRAS* data, given the angular resolution of *IRAS*, the sometimes large correction due to finite cloud radius, and the internal heating produced by embedded sources.

# APPENDIX

## ELLIPSE-FITTING PROCEDURE

We describe here our method of determining the ellipse that best approximates a closed two-dimensional curve, e.g., a contour level in a contour plot. Determining an ellipse means determining a complete set of parameters which unambiguously define that ellipse. In §§ 1 and 2 of this Appendix we describe two different sets of parameters completely defining an ellipse. The fitting procedure is described in § 3 below.

### 1. PARAMETERS DEFINING AN ELLIPSE

An ellipse is defined by five parameters. Given a coordinate system, these parameters can be chosen to be the coordinates of the center, $(x_0, y_0)$; the lengths of the semimajor and semiminor axes, $a$ and $b$; and the position angle $\theta$ of the major axis relative to some reference direction (e.g., $\theta$ with respect to the $x$-axis). The parametric equations of such an ellipse are

$$\begin{pmatrix} x \\ y \end{pmatrix} = \begin{pmatrix} x_0 \\ y_0 \end{pmatrix} + \begin{pmatrix} \cos\theta & -\sin\theta \\ \sin\theta & \cos\theta \end{pmatrix}\begin{pmatrix} a\cos\alpha \\ b\sin\alpha \end{pmatrix} , \tag{A1}$$

or

$$\begin{aligned} x &= x_0 + a\cos\theta\cos\alpha - b\sin\theta\sin\alpha , \\ y &= y_0 + a\sin\theta\cos\alpha + b\cos\theta\sin\alpha , \end{aligned} \tag{A1}$$

where $\alpha$ varies from 0 to $2\pi$ and represents the angular phase of a point on the ellipse, relative to the semimajor axis.

### 2. MOMENTS OF A DISTRIBUTION

Let us consider a two-dimensional closed curve $\{(x, y)\}$ and define the following two first-order moments, $\bar{x}$ and $\bar{y}$, and the three second-order moments, $V_x, V_y, V_{xy}$:

$$\bar{x} \equiv \oint x\, d\alpha \bigg/ \oint d\alpha , \tag{A2a}$$

$$\bar{y} \equiv \oint y\, d\alpha \bigg/ \oint d\alpha , \tag{A2b}$$

$$V_x \equiv \oint (x - \bar{x})^2\, d\alpha \bigg/ \oint d\alpha = \overline{x^2} - \bar{x}^2 , \tag{A2c}$$

$$V_y \equiv \oint (y - \bar{y})^2\, d\alpha \bigg/ \oint d\alpha = \overline{y^2} - \bar{y}^2 , \tag{A2d}$$

$$V_{xy} \equiv \oint (x - \bar{x})(y - \bar{y})\, d\alpha \bigg/ \oint d\alpha = \overline{xy} - \bar{x}\bar{y} . \tag{A2e}$$

Applied to the case of an ellipse whose parametric equations are given by $x(\alpha)$ and $y(\alpha)$ as in equations (A1), equations (A2) reduce to

$$\bar{x} \equiv \int_0^{2\pi} x \, d\alpha \Big/ \int_0^{2\pi} d\alpha = x_0 \, , \tag{A3a}$$

$$\bar{y} \equiv \int_0^{2\pi} y \, d\alpha \Big/ \int_0^{2\pi} d\alpha = y_0 \, , \tag{A3b}$$

$$V_x = \frac{a^2 \cos^2 \theta + b^2 \sin^2 \theta}{2} \, , \tag{A3c}$$

$$V_y = \frac{a^2 \sin^2 \theta + b^2 \cos^2 \theta}{2} \, , \tag{A3d}$$

$$V_{xy} = \frac{(a^2 - b^2) \cos \theta \sin \theta}{2} \, . \tag{A3e}$$

Inverting this system of equations, we obtain

$$x_0 = \bar{x} \, , \tag{A4a}$$

$$y_0 = \bar{y} \, , \tag{A4b}$$

$$a^2 = V_x + V_y + [(V_x - V_y)^2 + 4V_{xy}^2]^{1/2} \, , \tag{A4c}$$

$$b^2 = V_x + V_y - [(V_x - V_y)^2 + 4V_{xy}^2]^{1/2} \, , \tag{A4d}$$

$$\cos(2\theta) = \frac{V_x - V_y}{[(V_x - V_y)^2 + 4V_{xy}^2]^{1/2}} \, , \qquad \sin(2\theta) = \frac{2V_{xy}}{[(V_x - V_y)^2 + 4V_{xy}^2]^{1/2}} \, . \tag{A4e}$$

Equations (A3) indicate that the set of five parameters $\{\bar{x}, \bar{y}, V_x, V_y, V_{xy}\}$ composed of the two first-order moments and the three second-order moments, defined in equations (A2), is equivalent to the set $\{x_0, y_0, a, b, \theta\}$ defined in § 1 of this Appendix.

If the curve $C$ is given by a discrete set of $n$ points $\{(x_i, y_i)\}$ (e.g., a distribution of pixels), calculation of its moments is done by approximating equations (A2) with

$$\bar{x} \approx \frac{1}{n} \sum_{i=1}^{n} x_i \, , \tag{A5a}$$

$$\bar{y} \approx \frac{1}{n} \sum_{i=1}^{n} y_i \, , \tag{A5b}$$

$$V_x \approx \frac{1}{n} \sum_{i=1}^{n} x_i^2 - \bar{x}^2 \, , \tag{A5c}$$

$$V_y \approx \frac{1}{n} \sum_{i=1}^{n} y_i^2 - \bar{y}^2 \, , \tag{A5d}$$

$$V_{xy} \approx \frac{1}{n} \sum_{i=1}^{n} x_i y_i - \bar{x}\bar{y} \, . \tag{A5e}$$

### 3. ELLIPSE FITTING TO A CURVE

Given a curve $C$ to be fitted by an ellipse, we define the best-fitting ellipse as the ellipse which minimizes the expression

$$\chi^2 = \sum_i \left[ \frac{(x_i - x_0) \cos \theta + (y_i - y_0) \sin \theta}{a^2} + \frac{(y_i - y_0) \cos \theta + (x_i - x_0) \sin \theta}{b^2} - 1 \right]^2 \, .$$

This can be done using a nonlinear, five-dimensional least-squares fit. However, we have verified that, in most cases, the best-fitting ellipse coincides with the ellipse which has the same moments of the curve $C$.

Hence, it is generally sufficient to calculate the moments of $C$. The ellipse which has the same moments is almost always the best-fitting ellipse.

REFERENCES

Arquilla, R., & Goldsmith, P. F. 1985, ApJ, 297, 436
Bok, B. J., & Reilly, E. F. 1947, ApJ, 105, 255
Cernicharo, J., Bachiller, R., & Duvert, G. 1985, A&A, 149, 273
Chandrasekhar, S. 1957, in Stellar Structure (New York: Dover), 155
Chini, R., Krugel, E., & Kreysa, E. 1986, A&A, 167, 315
Clemens, D. P., & Barvainis, R. E. 1988, ApJS 68, 257 (CB)
Clemens, D. P., Yun, J. L., & Heyer, M. H. 1991, ApJS, 75, 877 (CYH)
Draine, B. T., & Lee, H. M. 1984, ApJ, 285, 89
Emerson, J. P. 1988, in Formation and Evolution of Low Mass Stars, ed. A. K.
    Dupree & M. T. V. T. Lago (Dordrecht: Kluwer), 21

Frerking, A. F., Langer, W. D., & Wilson, R. W. 1987, ApJ, 313, 320
Fulkerson, S. A., & Clark, F. O. 1984, ApJ, 287, 723
Heyer, M. H., Snell, R. L., Morgan, J., & Schloerb, F. P. 1989, ApJ, 346, 220
*IRAS* Catalogs and Atlases: Explanatory Supplement. 1988, ed. C. A. Beichman, G. Neugebauer, H. J. Habing, P. E. Clegg, & T. J. Chester (Washington, DC: GPO)
Langer, W. D., Wilson, R. W., Goldsmith, P. F., & Beichman, C. A. 1989, ApJ, 337, 355
Larson, R. B. 1969, MNRAS, 145, 271
Lee, M. H., & Roger, C. 1987, ApJ, 317, 197

Leung, C. M. 1985, in Protostars and Planets II, ed. S. C. Black & M. S. Matthews (Tucson: Univ. Arizona Press), 104
Leung, C. M., & O'Brien, E. V. 1989, ApJ, 337, 293
Penston, M. V. 1969, MNRAS, 144, 425
Shu, F. H. 1977, ApJ, 214, 488
Snell, R. L. 1981, ApJS, 45, 121
Tomita, Y., Saito, T., & Ohtani, H. 1979, PASJ, 31, 407
William, I. P., & Bhatt, H. C. 1982, MNRAS, 199, 465
Yun, J. L., & Clemens, D. P. 1990, ApJ, 367, L73